

Experimental and Computational Investigation of Progressive Damage Accumulation in CFRP Composites

Robert D. Crouch[†], Stephen B. Clay[‡] and Caglar Oskay^{†*}

[†]Department of Civil and Environmental Engineering
Vanderbilt University, Nashville, TN, 37235

[‡]Air Vehicles Directorate
Air Force Research Laboratory, WPFAB, OH 45433

Abstract

This manuscript presents an experimental and computational study of progressive damage accumulation in carbon fiber reinforced polymers. A series of monotonic tension experiments with acoustic emission, X-ray radiography, and X-ray computed tomography were performed on a quasi-isotropic layup to ascertain the initiation, progression, and modes of damage accumulation under tensile loading. A multiscale computational model was used to aid in understanding the progressive damage accumulation. The eigendeformation based reduced order homogenization modeling approach was used due to its computational efficiency and its ability to incorporate distinct damage modes. The combined experimental and computational investigation provided a detailed picture of the progression of damage accumulation in the CFRP composite. The multiscale model predictions were in good agreement with experimental observations.

Keywords: C. Multiscale modeling, C. Damage mechanics, D. Acoustic emission, D. X-Ray diffraction.

1 Introduction

The use of composite materials is growing at a significant pace in aerospace, marine, and other industries. Despite their rapidly expanding use and the significant body of research in the characterization of composites, achieving the capability to predict failure progression in structural applications remains an elusive goal.

One of the difficulties is that a multitude of failure mechanisms present at the scale of the material microstructure interact and contribute to the failure of a composite structure. For instance, diffuse microcracking within the matrix, fiber matrix debonding, delamination, fiber kinking, buckling and fracture are already well known and well characterized [1]. In addition, the mechanisms of failure and their interactions are strongly influenced by loading and stress states (e.g., tension, compression) as well as the damage state of the composite prior to loading (e.g., barely visible impact damage [2], compression-after-impact response [3]). Despite significant strides in modeling and experimental characterization of composite failure response, the interactions between various failure modes are not yet fully understood, and reliable prediction of progressive damage accumulation is still lacking.

Multiscale computational modeling is a promising approach for modeling failure in composites. The key characteristic of this approach is that damage accumulation is explicitly modeled by directly resolving and

*Corresponding Author: VU Station B#351831, 2301 Vanderbilt Place, Nashville, TN 37235. Email: caglar.oskay@vanderbilt.edu

numerically evaluating the microstructure response at each material point of a structural simulation. The effect of the failure processes modeled at the fine scale is transferred to the structural scale simulation based on scale bridging techniques such as computational homogenization [4], extended finite element method [5], generalized method of cells [6], multiscale finite element method [7], Voronoi cell finite element method [8], among others.

Damage and failure prediction cannot be achieved using computational modeling alone since such models rely on experiments for parameter calibration and validation. Several in-situ and post-mortem nondestructive inspection (NDI) methods, such as acoustic emission testing (AE), X-ray radiography, and X-ray computed tomography (CT), are instrumental in characterizing some aspects of damage progression and model validation. AE uses piezoelectric sensors to passively detect acoustic signals emitted by the material during damage propagation [9, 10]. The most advantageous characteristic of AE is that the sensors detect damage during testing in a range that cannot be distinguished by typical instrumentation such as load cells, strain gauges, and displacement transducers. X-ray radiography is a common NDI method, in which a two dimensional image is recorded on an imaging plate as energy is passed through a stationary material [1, 11]. In-plane delaminations can be easily detected due to the variation of X-ray absorption between the material and the void. The difficulty with X-ray radiography is the inability to characterize damage as a function of specimen thickness. X-ray CT provides an ultra-high resolution three dimensional image through the thickness of a material [12]. As X-ray CT equipment has become more readily available, this technique is being used for nondestructive evaluation of composites [13]. The primary advantage of X-ray CT for composite materials is that delaminations, transverse cracks, and fiber fracture can all be adequately characterized [14, 15].

This manuscript presents the first part of a two-part study on the progressive damage accumulation in carbon fiber reinforced polymer (CFRP) composites. The current manuscript details failure under monotonic loading conditions. The second part of the study addresses cyclic loading and is presented in a separate publication. A multiscale computational homogenization model [16] is employed to numerically characterize the progressive damage mechanisms of fiber fracture, matrix cracking, and delaminations as a function of loading. An experimental program using the combination of AE, X-ray radiography and X-ray CT techniques are employed to experimentally characterize the progression of damage throughout the loading history and assess the validity of the model predictions. A key contribution of this manuscript is that the sequencing and rate of failure at each ply of laminated composite specimens up to the sub-microstructure scale are established based on the combined experimental and computational investigation.

The remainder of this manuscript is organized as follows: Section 2 details the experimental program including the material fabrication, testing procedures and the NDI methods. Section 3 describes the computational model, the damage modes, and details of the numerical simulations. Section 4 presents the results of the experiments and computational simulations. The conclusions are provided in Section 5.

2 Experimental Procedures

A series of monotonic tension tests were conducted on the graphite fiber reinforced epoxy, IM7/977-3. In-situ acoustic emission monitoring was used to characterize damage propagation with increasing load. X-ray radiography and X-ray CT were used periodically to visually inspect the type, location, and extent of internal damage.

2.1 Material Fabrication

Composite panels were hand laid from unidirectional preimpregnated IM7/977-3 graphite epoxy. 0° , 90° , and quasi-isotropic ($[+45, 0, -45, 90]_{2s}$) panels were made. They were cured in an autoclave at a temperature of 177°C and a pressure of 689 kPa. After cure, the panels were cut into multiple test specimens. The number of replicates, the number of plies, and the nominal dimensions of the specimens are shown in Table 1. Acid digestion testing determined the mean fiber volume fraction of the specimens to be 66.6% with a standard deviation of 2.5%.

2.2 Testing

Two sets of monotonic tension tests were conducted on an MTS universal testing machine according to ASTM D3039 [17]. Both sets of tension tests were conducted at a constant displacement rate of 1.27 mm/min. The first set of tests was conducted on 0° and 90° unidirectional composite specimens, and the second set of tests was conducted on quasi-isotropic specimens. The mean and standard deviation of the modulus and failure stress of all tested specimens are summarized in Table 2.

Damage progression was thoroughly characterized on a single quasi-isotropic specimen utilizing acoustic emission, X-ray radiography, and X-ray computed tomography. These non-destructive experimental techniques revealed the quantity and location of damage as a function of load. The specimen was loaded at a slower displacement rate (0.127 mm/min) to better capture the acoustic emission hits as a function of time. The specimen was unloaded and reloaded for damage characterization at 300 MPa, 400 MPa, 620 MPa, 710 MPa, 845 MPa, and at failure (846 MPa). We unloaded the specimen when the acoustic emission hit count, which was monitored in real-time, accelerated. After each unloading, X-ray radiography was employed to visualize the state of damage. After unloading from 710 MPa and 845 MPa, X-ray CT was also used to obtain three dimensional images of the damage state.

2.3 Acoustic Emission

In-situ acoustic emission (AE) activity was recorded on a Micro-II Digital AE System produced by Physical Acoustics Corporation. When a material experiences local failure, it releases strain energy which produces a stress wave in the specimen. The AE system detects this acoustic energy and records it as a *hit*. Prior to testing, an AE calibration study was performed to define the appropriate signal conditioning parameters. It was found that an amplitude threshold of 48 dB enabled the detection of all valid material failure events without recording ambient noise. As recommended by the equipment manufacturer, the AE timing parameters used for this study were peak definition time = 400 μs , hit definition time = 800 μs , hit lockout time = 200 μs , and maximum duration = 100 ms.

2.4 X-ray Radiography

The specimen was examined using a 160 kV Philips X-ray system (0.4 mm focal spot) and General Electric CR Tower Computed Radiography system using IPS imaging plates and 50 micron sampling. The imaging parameters were 26 kV, 3 mA, and 30 s, with a source-to-detector distance of 122 cm. Prior to X-ray examination, the edges of the specimen were exposed to zinc iodide, an opaque penetrant, which was absorbed into all cracks and voids adjacent to the specimen edge. The optimum view of damage was achieved using the General Electric Rhythm image processing software where a level III contrast enhancement filter was applied to each X-ray image using noise reduction and latitude correction.

2.5 X-ray Computed Tomography

The specimen was examined using an X-Tek HMX160 CT system. The main components included an X-ray source, a rotation stage on which the sample was fixed, and an X-ray detector. The maximum resolution, at highest magnification, was approximately $5 \mu\text{m}$. A Molybdenum target was used. The source voltage and the source current were 90 kV and $90 \mu\text{A}$, respectively. The specimen was clamped vertically approximately 33 cm from the X-ray source. The sample rotates over 360° with a step size of 0.5° . Averages of eight projection images (1024×1024 pixels) were collected at each position. The raw image data was reconstructed using CT Pro software. Three dimensional structure of the damaged specimen was visualized in order to evaluate the damage through the thickness of the specimen using 3D surface rendering techniques.

3 Computational Model

The geometry, finite element discretization, and boundary conditions considered in the specimen model are illustrated in Fig. 1. The length, width, and thickness of the numerical model were 6 mm, 25 mm, and 1 mm, respectively. The discretization of the model consisted of 26,560 trilinear hexahedral elements. Only the top half of the specimen was discretized due to the symmetry of the quasi-isotropic layup by employing symmetric boundary conditions at the bottom face of the numerical specimen. Each of the 8 modeled plies was explicitly meshed with 2 elements along the thickness dimension. Local material orientations were prescribed in the specimen model to account for the different ply orientations. A small part of the specimen along the length ($L=6$ mm) was modeled to reduce the computational cost of the simulations. Periodic boundary conditions were imposed along the y-direction to eliminate spurious boundary effects due to submodeling. The length of the numerical specimen (6 mm) was chosen to be greater than (more than three times) the observed average distance between cracks in the experimental specimen (measured as 1.6 mm for 45° plies and 0.5 mm for 90° plies) to avoid interaction of damage effects between the top and bottom edges. The specimen was loaded by increasing the average distance between the top and bottom edges using constraints. The magnitude of the applied stress was taken to be the total constraint force required to maintain the specified average distance between the specimen ends divided by the cross sectional area of the specimen.

3.1 Multiscale Failure Modeling

Computational homogenization (CH) with multiple spatial scales [18] was used to model the mechanical response and failure in the composite specimens. In the CH method the constitutive response at the material point of a macroscopic (i.e. specimen) model is provided by numerically evaluating a microscale model of the representative volume or a unit cell of the composite. Spatial averaging (i.e. homogenization) of the microscale response yields the constitutive relationship between the macroscopic stress and deformation. Therefore, no explicit constitutive form is assumed to describe the composite level response. Since damage is considered directly at the scale of the constituents, damage modes such as fiber cracking, transverse cracking, and delamination are a natural consequence of the microscale response and explicitly evaluated within the multiscale model.

The requirement of evaluating a full microstructure model in CH typically leads to very high computational costs. In this study, we employ the eigendeformation-based reduced order homogenization method (EHM) [16] to efficiently evaluate the response at the scale of the microstructure. The EHM model employs transformation field analysis [19] to reduce the computational complexity, by precomputing certain information (e.g., localization operators, influence functions, and concentration tensors) regarding the microstructure response through evaluating linear elastic unit cell problems before analyzing the macroscale structure.

The unit cell of the CFRP composite material within a single ply is shown in Fig. 2. The unit cell consists of the unidirectional fiber and the epoxy resin. Consider the partitioning of the unit cell domain into n parts within which the strains and damage are assumed to be spatially constant. Let $D^{(\alpha)}$ be a scalar damage variable indicating the state of damage within part α :

$$\boldsymbol{\sigma}^{(\alpha)} = (1 - D^{(\alpha)})\mathbf{L}^{(\alpha)} : \boldsymbol{\varepsilon}^{(\alpha)} \quad (1)$$

in which $\boldsymbol{\varepsilon}^{(\alpha)}$ and $\boldsymbol{\sigma}^{(\alpha)}$ are the average strain and stress within part α , $\mathbf{L}^{(\alpha)}$ is the tensor of elastic moduli of the constituent material occupying part α , and ":" denotes the double inner product of two high order tensors. The evolution of $D^{(\alpha)}$ as a function of loading is modeled as:

$$D^{(\alpha)} = \Phi(v_{\max}^{(\alpha)}) \quad (2)$$

where $v_{\max}^{(\alpha)}$ is defined as:

$$v_{\max}^{(\alpha)}(t) = \max_{0 \leq \tau \leq t} \{v^{(\alpha)}(\tau)\} \quad (3)$$

in which $v^{(\alpha)}$ is the damage equivalent strain in part α :

$$v^{(\alpha)} = \sqrt{\frac{1}{2}\boldsymbol{\varepsilon}^{(\alpha)} : \mathbf{L}^{(\alpha)} : \boldsymbol{\varepsilon}^{(\alpha)}} \quad (4)$$

The phase damage evolution function is modeled using a two-parameter arctangent law:

$$\Phi(v^{(\alpha)}) = \frac{\arctan(a^{(\alpha)}v^{(\alpha)} - b^{(\alpha)}) + \arctan(b^{(\alpha)})}{\frac{\pi}{2} + \arctan(b^{(\alpha)})} \quad (5)$$

in which $a^{(\alpha)}$ and $b^{(\alpha)}$ are material parameters controlling the brittleness of failure and material strength, respectively. Figure 3 schematically illustrates the effect of parameters $a^{(\alpha)}$ and $b^{(\alpha)}$ on constituent material stress-strain response. The macroscale stress, $\bar{\boldsymbol{\sigma}}$, of the overall fiber reinforced composite ply is expressed in terms of the macroscale strain, $\bar{\boldsymbol{\varepsilon}}$, the phase averaged damage induced inelastic strains, $\boldsymbol{\mu}^{(\alpha)}$, and the average phase damage, $D^{(\alpha)}$, as:

$$\bar{\boldsymbol{\sigma}} = \sum_{\Delta=1}^n \left\{ \left(1 - D^{(\Delta)}\right) \left(\mathbf{F}^{(\Delta)} : \bar{\boldsymbol{\varepsilon}} + \sum_{\alpha=1}^n \mathbf{H}^{(\Delta\alpha)} : \boldsymbol{\mu}^{(\alpha)} \right) \right\} \quad (6)$$

The eigenstrains, $\boldsymbol{\mu}^{(\alpha)}$, are obtained by solving the following nonlinear system of equations:

$$\sum_{\Delta=1}^n \left\{ \left(1 - D^{(\Delta)}\right) \left(\mathbf{A}^{(\alpha\Delta)} : \bar{\boldsymbol{\varepsilon}} + \sum_{\beta=1}^n \mathbf{B}^{(\alpha\Delta\beta)} : \boldsymbol{\mu}^{(\beta)} \right) \right\} = \mathbf{0}, \quad \alpha = 1, \dots, n \quad (7)$$

The coefficient tensors $\mathbf{A}^{(\alpha\Delta)}$, $\mathbf{B}^{(\alpha\Delta\beta)}$, $\mathbf{F}^{(\Delta)}$, and $\mathbf{H}^{(\Delta\alpha)}$ are expressed as:

$$\mathbf{A}^{(\eta\Delta)} = \int_{\Theta^{(\Delta)}} \mathbf{P}_{\top}^{(\eta)}(\mathbf{y}) : \mathbf{L}(\mathbf{y}) : (\mathbf{I} + \mathbf{G}(\mathbf{y})) d\mathbf{y} \quad (8)$$

$$\mathbf{B}^{(\eta\Delta\gamma)} = \int_{\Theta^{(\Delta)}} \mathbf{P}_{\top}^{(\eta)}(\mathbf{y}) : \mathbf{L}(\mathbf{y}) : \mathbf{P}^{(\gamma)}(\mathbf{y}) d\mathbf{y} \quad (9)$$

$$\mathbf{F}^{(\Delta)} = \frac{1}{|\Theta|} \int_{\Theta^{(\Delta)}} \mathbf{L}(\mathbf{y}) : (\mathbf{I} + \mathbf{G}(\mathbf{y})) d\mathbf{y} \quad (10)$$

$$\mathbf{H}^{(\Delta\gamma)} = \frac{1}{|\Theta|} \int_{\Theta^{(\Delta)}} \mathbf{L}(\mathbf{y}) : \mathbf{P}^{(\gamma)}(\mathbf{y}) d\mathbf{y} \quad (11)$$

$$\mathbf{P}^{(\Delta)}(\mathbf{y}) = \int_{\Theta^{(\Delta)}} \mathbf{g}_{\text{ph}}(\mathbf{y}, \hat{\mathbf{y}}) d\hat{\mathbf{y}} \quad (12)$$

where Θ and $\Theta^{(\alpha)}$ are the domains of the RVE and the domain of part α , respectively, and \mathbf{g}_{ph} and \mathbf{G} are the damage-induced and elastic polarization functions computed from particular solutions of the unit cell problem. Subscript \top denotes transpose, and \mathbf{I} is the fourth order symmetric identity tensor.

The partitioning of the unit cell employed in the present investigation is shown in Fig. 2c. The partitioning captures three distinct failure modes: fiber failure ($\alpha = 1$), transverse cracking ($\alpha = 2$), and delamination ($\alpha = 3$). Part 4 ($\alpha = 4$) is common to transverse cracking and delamination, which is introduced to treat intersecting failure paths. For instance, full damage within part 1 ($D^{(1)} = 1$) indicates complete loss of load carrying capacity of the fiber phase (i.e., fiber failure), whereas, $D^{(3)} = D^{(4)} = 1$ indicates full separation between two plies (i.e., delamination). Within the current multiscale computational framework, it is also possible to explicitly model interfacial decohesion [20]. Unfortunately, experimental data to fully characterize the interfacial behavior is currently unavailable. The matrix parameters are

calibrated to account for the combined effect of interfacial decohesion and diffuse matrix cracking.

The evolution of each damage mode is tracked separately by using the damage evolution form in Eqs. 1-5. This is identified by using superscript (α) in the damage evolution equations. Therefore, each damage mode is allowed to propagate along its preferred direction. It must be noted that the damage modes are coupled to each other to ensure that microstructural equilibrium is satisfied. The damage modes are coupled through the polarization functions.

3.2 Calibration of the Model Parameters

The elastic and damage properties of the constituent materials (i.e. fiber and matrix) were calibrated using experiments conducted on 0° and 90° unidirectionally stacked specimens, as well as experimental data available in the literature. In the model, a uniform distribution of fibers was assumed. The variability of specimen strength seen in the 0° calibration experiments is partially due to nonuniform fiber distribution, but as the primary concern in this work is tensile loading, it is assumed the effect of nonuniform fiber distribution is limited.

The 977-3 resin was taken to be isotropic with elastic modulus, $E^{(m)}$, and Poisson's ratio, $\nu^{(m)}$. The IM7 fiber was assumed to be transversely isotropic with elastic material properties denoted as $E_1^{(f)}$, $E_2^{(f)}$, $G_{12}^{(f)}$, $\nu_{12}^{(f)}$, and $\nu_{23}^{(f)}$. The Poisson's ratios of the resin and fiber were set as $\nu^{(m)} = 0.35$ [21], $\nu_{12}^{(f)} = 0.32$, and $\nu_{23}^{(f)} = 0.20$ [22]. The constituents' elastic moduli, $E^{(m)}$, $E_1^{(f)}$, $E_2^{(f)}$, and $G_{12}^{(f)}$, were calibrated by minimizing the discrepancy between the composite elastic moduli of 0° and 90° specimens and the simulated elastic moduli of the homogenized composite. The constituent moduli were determined as $E^{(m)} = 3.55$ GPa, $E_1^{(f)} = 263$ GPa, $E_2^{(f)} = 13$ GPa, and $G_{12}^{(f)} = 27.5$ GPa which were in close agreement with previous investigations [21, 22].

The model parameters that define damage accumulation are $a^{(f)}$ and $b^{(f)}$ for the fiber and $a^{(m)}$ and $b^{(m)}$ for the matrix. The fiber damage accumulation parameters are calibrated based on the set of experiments conducted on unidirectional 0° specimens. The fiber constituent parameters are identified by minimizing the discrepancy between experimentally observed stress-strain response and numerical predictions of the multiscale model in the least squares sense (Fig. 4). The fiber parameters were calibrated so that the model response equals the average experimental strength observed in the 0° specimens. The matrix parameters were calibrated in a similar manner using the manufacturer provided resin strength [23] and the set of experiments conducted on unidirectional 90° specimens. A mean matrix strength of 114 MPa is employed. The calibrated model parameters were $a^{(f)} = 0.05$, $b^{(f)} = 340$, $a^{(m)} = 0.002$, and $b^{(m)} = 4.0$.

4 Results and Discussion

Figure 5 shows the number of cumulative hits and the cumulative energy as a function of applied stress amplitude measured in the AE testing at each load increment. Cumulative energy weighs each recorded hit based on the magnitude of the strain energy released during the damage event. When the specimen is unloaded and reloaded, the cumulative hits and energy remained relatively flat until the past maximum loading magnitude was exceeded indicating insignificant cyclic damage accumulation with the exception of

the loading to 845 MPa. An increase in the recorded AE hits (Figure 5a) was observed at approximately 400 MPa, whereas AE cumulative energy (Figure 5b) displayed an increase at approximately 600 MPa suggesting initiation of damage growth within the specimen at this range of loading. Damage progressively accumulates, signaled by an increasing rate of AE cumulative energy, until the ultimate failure. In contrast with the transverse cracking at lower loading magnitudes, the cracking events near ultimate failure (starting around 80% of the ultimate load) were audible without any listening aides.

While AE testing provides qualitative information about the progressive nature of damage accumulation, the type and location of failure associated with an acoustic hit is less clear. The frequency and amplitude of recorded waves does provide some degree of information on the nature of the failure event such as fiber fracture and matrix damage [24], but more detailed information such as damage in individual plies is difficult to gather from AE measurements alone. X-ray radiography and X-ray CT provide snapshots of the location and type of accumulated damage within the specimen. An X-ray radiograph was taken at loading amplitudes of 0 MPa (pristine specimen), 300 MPa, 400 MPa, 620 MPa, 710 MPa, and 845 MPa. As illustrated in Figure 6, the cracks appear in light color in the X-ray radiographs due to the presence of the dye penetrant. No substantial cracks were visible for the first two loadings of 300 MPa and 400 MPa other than minor edge imperfections. At a loading of 620 MPa, visible cracks formed with orientations both perpendicular and $\pm 45^\circ$ to the loading direction. Between 620 MPa and 710 MPa, the number and length of cracks increased. At a loading of 845 MPa (ultimate failure: 846 MPa), a large delamination was observed on the lower left side of the specimen (Fig. 6f) with smaller delaminations present on both sides of the specimen. We note that the dye penetrant was applied to the outer faces of the specimen. Internal cracks, that were unconnected to the outer faces and not penetrated by the dye, are therefore invisible to the X-ray radiography imaging.

X-ray CT was employed to obtain a 3-D visualization of the extent and mechanisms of damage within the specimen. Figure 7 illustrates the 3-D tomographic image of the specimen at 710 MPa and 845 MPa. Extensive 45° and 90° cracks are evident as well as delaminations along the length of the specimen edge. Figure 8 illustrates the layer-by-layer damage profile observed using the X-ray computed tomography. The 0° ply shown in Fig. 8a exhibited some degree of debonding in the fiber direction. In contrast to X-ray radiography, the tomographic images are able to capture internal cracks that are not exposed to the dye-penetrant (Fig. 8a). The 90° ply at the center of the specimen developed extensive transverse cracking extending across the width of the specimen. In addition to transverse cracking, delaminations were observed at the specimen edges. The 45° ply (the top ply of the specimen) shown in Fig. 8c developed extensive cracking across the specimen width along with delaminations at the specimen edges. The large delamination shown in the radiograph of Fig. 6d cannot be seen in Fig. 8 since the tomographic images were taken over a smaller region of the specimen outside of the large delamination.

The calibrated computational model described in Section 3 was employed to gain further understanding of the progressive damage accumulation in the specimen. Figure 9a shows the stress-strain response of the

virtual specimen under monotonic tensile loading. The predicted stress-strain response of the overall composite is displayed alongside the cumulative energy versus stress curve recorded by the AE system seen in Fig. 9b (the energy was summed over all loadings). The ultimate strength of the specimen predicted by the model was 887 MPa which was in good agreement with the experimentally observed mean strength of 872 MPa with a standard deviation of 30 MPa. The strength of the specimen probed by the NDI techniques was 846 MPa. The ultimate failure was caused by fiber fracture in the 0° plies in both the numerical investigation and the experiments.

In the numerical simulations, the first major compliance change (Fig. 9a) takes place at approximately 591 MPa when transverse cracking propagates in the top 45° ply. The compliance change in the virtual specimen coincides with the increase in AE cumulative energy illustrated in Fig. 9b, which occurs at approximately 600 MPa. The X-ray radiograph taken at 620 MPa (Fig. 6c) displays damage within the specimen, whereas no discernable damage was observed in the radiograph taken at 400 MPa (Fig. 6b) confirming that the damage initiation prediction of the model is in reasonable agreement with the experimental observations.

Figures 10 and 11 compares the damage contours predicted by the numerical simulations to the X-ray radiographs taken at 620 MPa and 710 MPa, respectively. Qualitatively, the evolution of damage predicted by the numerical simulations is in good agreement with the experimental observations. The matrix cracks that initiated at the $\pm 45^\circ$ plies rapidly propagate across the length of the specimen. The progression of damage in the inner $\pm 45^\circ$ plies occurs less rapidly with cracking reaching across the entire width of the specimen at 698 MPa. The difference in speed of damage progression is attributed to the confinement of the inner $\pm 45^\circ$ plies compared to the top ply, which retards crack growth. The computed tomography images taken at 710 MPa and 845 MPa (Fig. 7) appear to be consistent with observations of the simulation that faster and consequently more dominant cracking is observed at the outer $\pm 45^\circ$ plies. Further investigations are planned to independently confirm this finding. Matrix cracking within the $\pm 45^\circ$ plies is followed by the initiation of damage within the 90° plies between 587 MPa (when damage first initiates in the 90° ply) and 623 MPa (when damage initiates in all 90° plies). Cracking extended across the entire width of the virtual specimen within the 90° plies between 721 MPa and 773 MPa. The 90° cracks clearly initiate from the specimen edges. Matrix cracking in the 0° plies remains negligible until the loading reaches close to the ultimate failure strength of the specimen.

The initiation of delamination within the specimens occurs slightly after the initiation of matrix cracking. Small edge delaminations initiate at 511 MPa. The edge delaminations continue to grow slowly until the loading reaches close to the ultimate strength of the specimen. This observation is in close agreement with the high rate of increase in the AE cumulative energy at the later stages of loading to the progression of delaminations as shown in Fig. 9b. X-ray radiographs and tomographs confirm this observation as well. Figure 12 illustrates edge delaminations at 845 MPa. The failure patterns predicted by the model shown in Figs. 10-12 are in good agreement with the patterns observed in the tomographic

images in Fig. 8.

5 Conclusions

This manuscript provided a comprehensive experimental/computational investigation of progressive damage accumulation in CFRP composites subjected to monotonic loading. The acoustic emission, X-ray radiography, and X-ray computed tomography inspection methods were used to obtain a clear picture of the evolution of damage within the composite in terms of cracking and delamination events as a function of loading. The multiscale computational model was employed to gain further insight into the interaction and sequencing of damage mechanisms which was difficult to capture using any of the experimental techniques. The response mechanisms captured by the model predictions and the experimental observations were in reasonable agreement.

Next, we will employ the current experimental/computational methodologies to investigate damage mechanisms and progressive failure under cyclic loading conditions. Fatigue damage accumulation presents additional challenges particularly in computational modeling including establishing effective time stepping strategies to describe the accumulation of damage as a function of loading cycles, as well as accounting for the loading frequency and temperature effects. These modeling issues will be addressed in the near future.

6 Acknowledgments

The authors gratefully acknowledge the financial support and experimental facilities provided by the Air Vehicles Directorate of the Air Force Research Laboratory (Contract No: F3446-09-46-SC01-01 through General Dynamics Information Technology Inc.). We also acknowledge the Air Force Research Laboratory Materials and Manufacturing Directorate for access to radiography and computed tomography technology.

References

- [1] W.W. Stinchcomb. Nondestructive evaluation of damage accumulation processes in composite laminates. *Compos. Sci. Technol.*, 25:103–118, 1986.
- [2] P. Kumar and B. Rai. Delaminations of barely visible impact damage in CFRP laminates. *Compos. Struct.*, 23:313–318, 1993.
- [3] H. Yan, C. Oskay, A. Krishnan, and L. R. Xu. Compression after impact response of woven fiber reinforced composites. *Compos. Sci. Technol.*, 70:2128–2136, 2010.
- [4] J. Fish and Q. Yu. Multiscale damage modelling for composite materials: Theory and computational framework. *Int. J. Numer. Meth. Engng.*, 52:161–191, 2001.
- [5] T. B. Belytschko, S. Loehnert, and J. H. Song. Multiscale aggregating discontinuities: a method for circumventing loss of material stability. *Int. J. Numer. Meth. Engng.*, 73:869–894, 2008.

- [6] J. Aboudi. The generalized method of cells and high-fidelity generalized method of cells micromechanical models — a review. *Mechanics of Advanced Materials and Structures*, 11:329–366, 2004.
- [7] T. Y. Hou and X.-H. Wu. A multiscale finite element method for elliptic problems in composite materials and porous media. *J. Comput. Physics*, 134:169–189, 1997.
- [8] S. Ghosh. *Micromechanical Analysis and Multi-Scale Modeling Using the Voronoi Cell Finite Element Method*. Taylor & Francis, 2011.
- [9] A.A. Pollock. Loading and stress in acoustic emission testing. *Mater. Eval.*, 2004.
- [10] C.J. Hellier. *Handbook of Nondestructive Evaluation*. McGraw-Hill, 2001.
- [11] K.T. Tan, N. Watanabe, and Y. Iwahori. X-ray radiography and micro-computed tomography examination of damage characteristics in stitched composites subjected to impact loading. *Composites Part B*, 42:874–884, 2011.
- [12] S.R. Stock. X-ray microtomography of materials. *Int. Mater. Rev.*, 44:141–164, 1999.
- [13] F. Sket, R. Seltzer, J.M. Molina-Aldareguia, C. Gonzalez, and J. Llorca. Determination of damage micromechanisms and fracture resistance of glass fiber/epoxy cross-ply laminate by means of X-ray computed microtomography. *Compos. Sci. Technol.*, 72:350–359, 2012.
- [14] J.P. Dunkers, D.P. Sanders, D.L. Hunston, M.J. Everett, and W.H. Green. Comparison of optical coherence tomography, x-ray computed tomography, and confocal microscopy results from an impact damaged epoxy/e-glass composite. *J. Adhes.*, 78:129–154, 2002.
- [15] D.D. Symons. Characterisation of indentation damage in 0/90 layup T300/914 CFRP. *Compos. Sci. Technol.*, 60:391–401, 2000.
- [16] R. Crouch and C. Oskay. Symmetric meso-mechanical model for failure analysis of heterogeneous materials. *Int. J. Mult. Comp. Eng.*, 8:447:461, 2010.
- [17] ASTM Standard D3039M-08. Standard test method for tensile properties of polymer matrix composite materials. *Annual Book of ASTM Standards*, 2008.
- [18] J.M. Guedes and N. Kikuchi. Preprocessing and postprocessing for materials based on the homogenization method with adaptive finite element methods. *Comput. Meth. Appl. Mech. Eng.*, 83:143–198, 1990.
- [19] G.J. Dvorak. Transformation field analysis of inelastic composite materials. *Proc. R. Soc. Lond. A*, 437:311–327, 1992.

- [20] C. Oskay and J. Fish. Eigendeformation-based reduced order homogenization for failure analysis of heterogeneous materials. *Comp. Meth. Appl. Mech. Engng.*, 196(7):1216–1243, 2007.
- [21] J.R. Gregory and S.M. Spearing. Constituent and composite quasi-static and fatigue fracture experiments. *Compos. Part. A-Appl. S.*, 36:665–674, 2005.
- [22] T. Breitzman, R. Lipton, and E. Iarve. Local field assessment inside multiscale composite architectures. *Multiscale Model. Simul.*, 6:937–962, 2007.
- [23] AECM-00036 Rev: 01. Cycom 977-3 Epoxy Resin System Technical Data Sheet.
http://www.cemselectorguide.com/pdf/CYCOM_977-3_031912.pdf, March 19, 2012.
- [24] A. Bussiba, M. Kupiec, S. Ifergane, R. Piat, and T. Bohlke. Damage evolution and fracture events sequence in various composites by acoustic emission technique. *Compos. Sci. Technol.*, 68:1144–1155, 2008.

Figure Captions

Figure 1: Quasi-isotropic specimen model.

Figure 2: Partitioning of the unidirectionally reinforced composite unit cell.

Figure 3: Stress-strain curves produced by the two parameter arctangent law: (a) $a^{(\alpha)}$ is varied while $b^{(\alpha)}$ is set to maintain constant failure stress (b) $b^{(\alpha)}$ was varied while maintaining constant $a^{(\alpha)}$.

Figure 4: The stress-strain response of the calibrated model compared with experimental data for specimens with 0° layup.

Figure 5: Loading stress versus (a) cumulative AE hits and (b) cumulative AE energy.

Figure 6: X-ray radiographs after loading to (a) 0 MPa (b) 400 MPa (c) 620 MPa (d) 845 MPa.

Figure 7: 3D tomographic images of damage in the specimen at a loading of (a) 710 MPa (b) 845 MPa (c) 845 MPa (rotated view).

Figure 8: Computed tomography scans after loading to 845 MPa: (a) second 0° ply from bottom (b) central 90° ply (c) top 45° ply.

Figure 9: (a) Stress-strain for the quasi-isotropic specimen model (b) cumulative energy vs. stress for the experimental quasi-isotropic specimen recorded by AE.

Figure 10: Damage profiles at 620 MPa loading: (a) experimental (b) top (45°) ply (simulated) (c) the center (90°) ply of the specimen (simulated).

Figure 11: Damage profiles at 710 MPa loading: (a) experimental (b) top (45°) ply (simulated) (c) the center (90°) ply of the specimen (simulated).

Figure 12: Damage profiles at 845 MPa loading: (a) experimental (b) delaminations for all plies.

Fiber Orientation	Number of Replicates	Number of Plies	Length [mm]	Width [mm]	Thickness [mm]
0°	13	8	250	13	1
90°	17	16	177	25	2
Quasi-Iso.	7	16	250	25	2

Table 1: Details of the IM7/977-3 specimens.

Fiber Orientation	Tensile Modulus [GPa]	Failure Stress [MPa]
0°	158 (13)	2,841 (296)
90°	8.644 (0.712)	63 (14)
Quasi-Iso.	60.7 (2.2)	872 (30)

Standard deviation shown in parentheses.

Table 2: Modulus and strength of IM7/977-3 specimens.

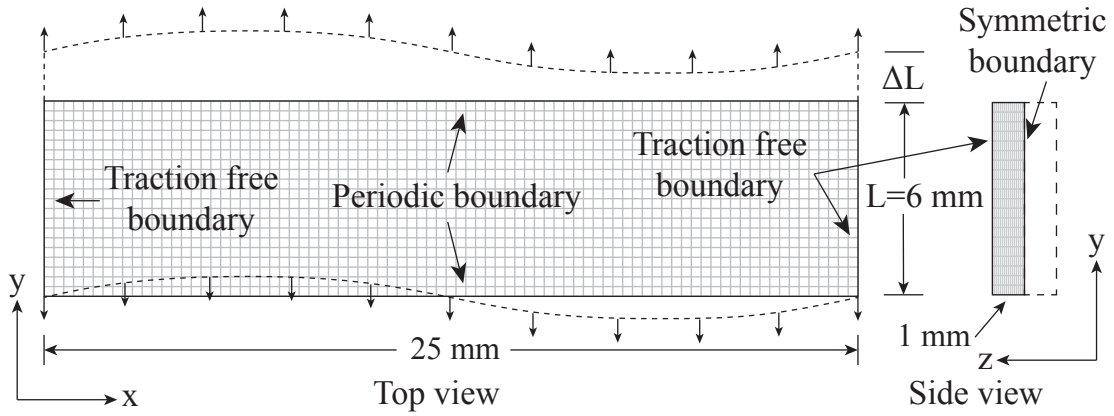


Figure 1:

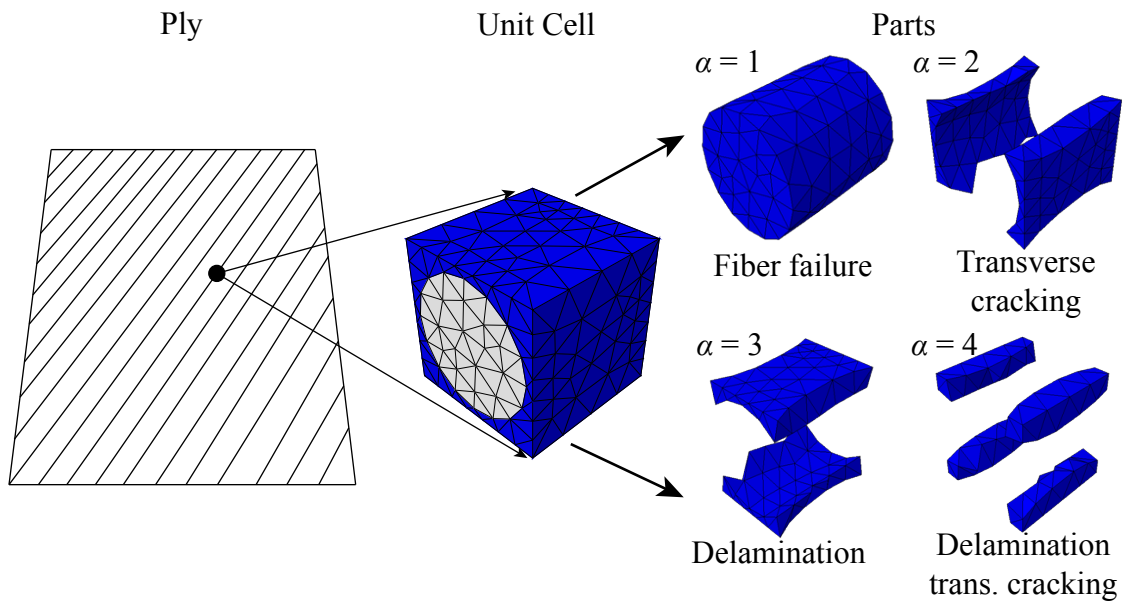


Figure 2:

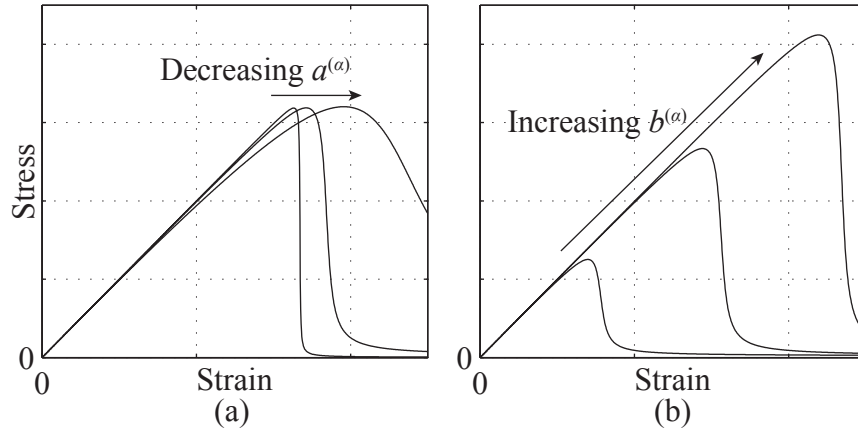


Figure 3:

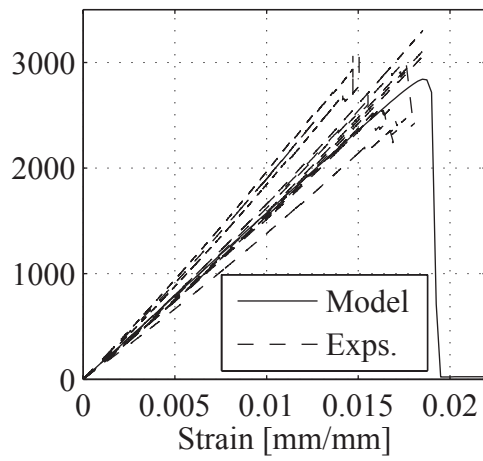


Figure 4:

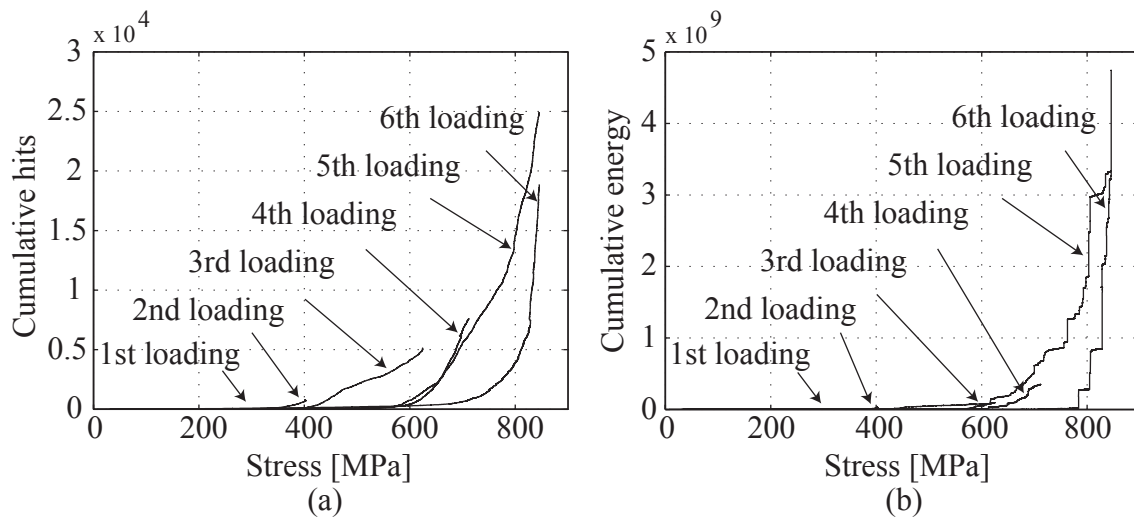


Figure 5:

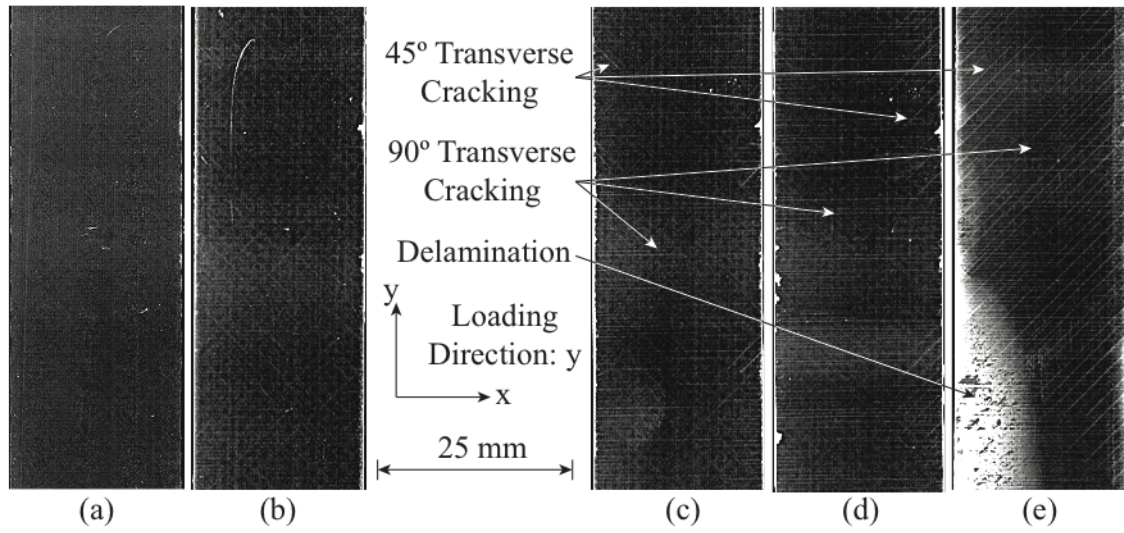


Figure 6:

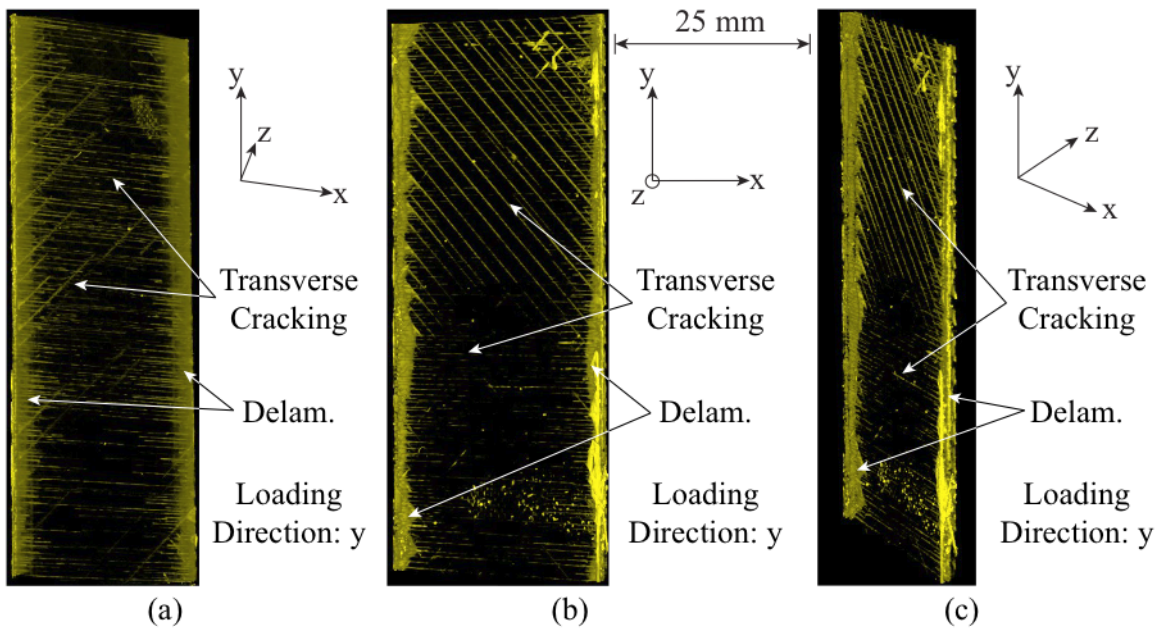


Figure 7:

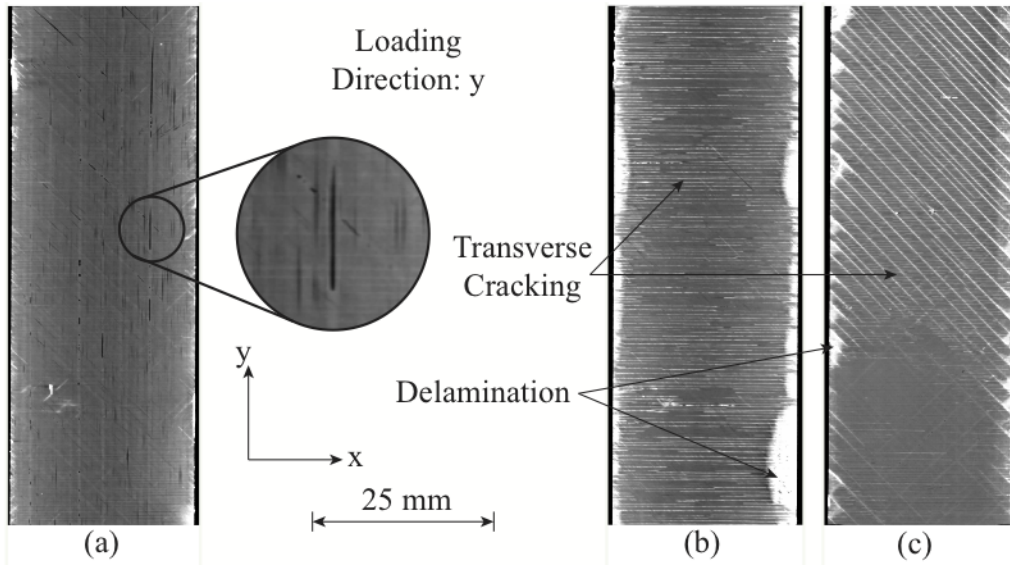


Figure 8:

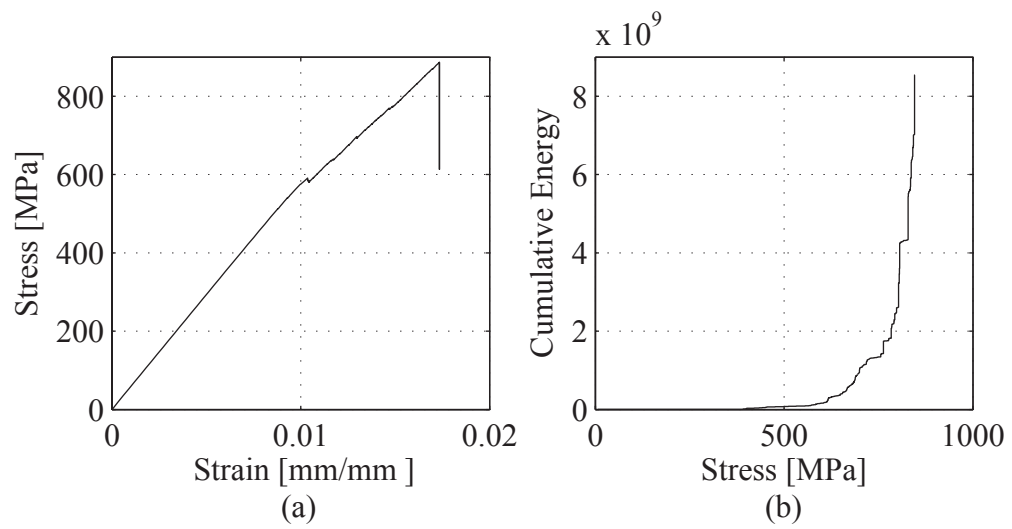


Figure 9:

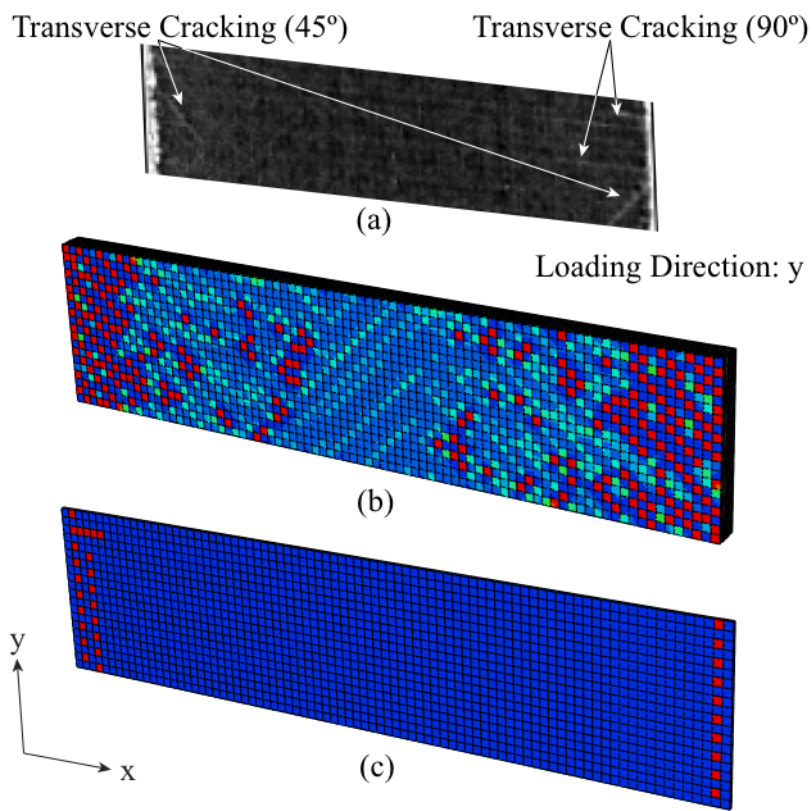


Figure 10:

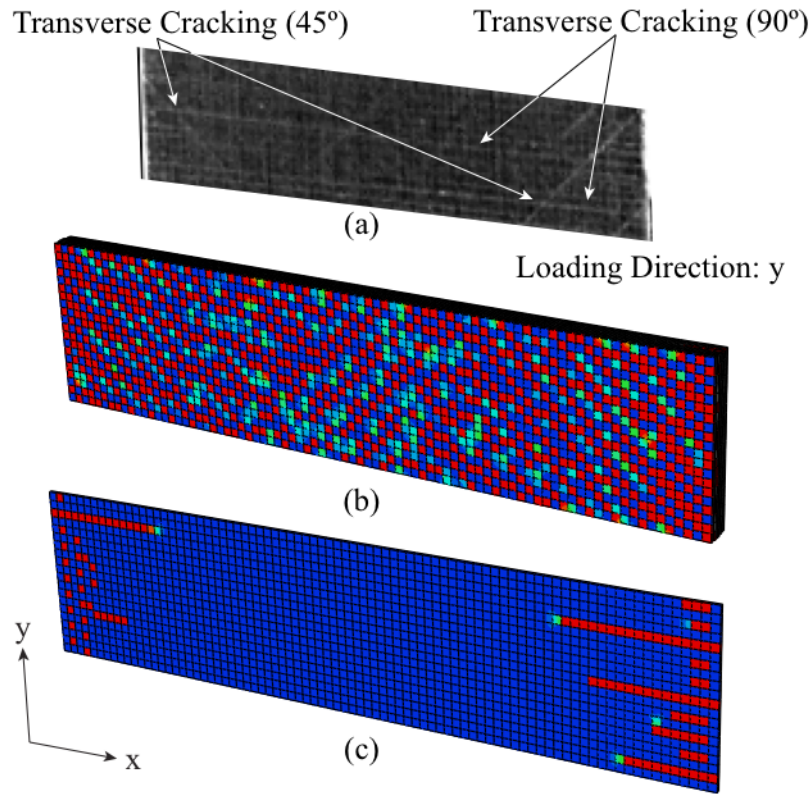


Figure 11:

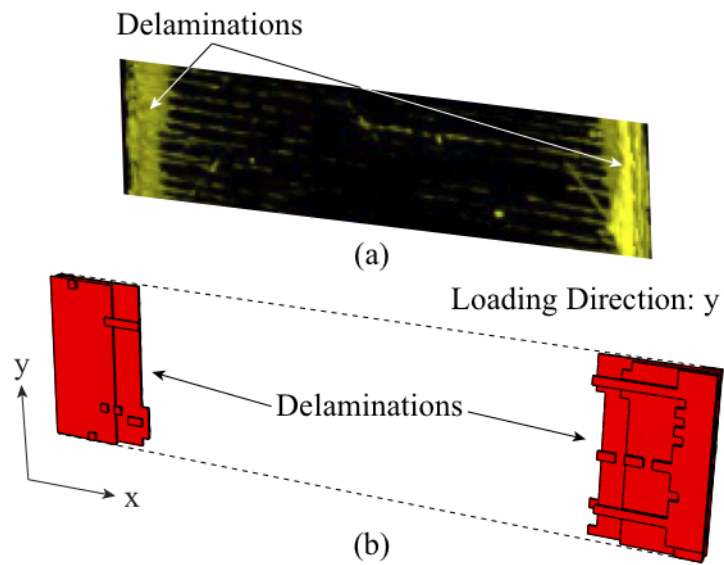


Figure 12: